Acta Materialia 238 (2022) 118241

Contents lists available at ScienceDirect

Acta Materialia

journal homepage: www.elsevier.com/locate/actamat

Full length article

A new healing strategy for metals: Programmed damage and repair

Mariia Arseenko[a], Florent Hannard[a], Lipeng Ding[a,b,c], Lv Zhao[a,d], Eric Maire[e], Julie Villanova[f], Hosni Idrissi[a,b], Aude Simar[a,*]

[a] Institute of Mechanics, Materials and Civil Engineering, UCLouvain, Louvain-la-Neuve 1348, Belgium
[b] Electron Microscopy for Materials Science, University of Antwerp, Antwerp 2000, Belgium
[c] Key laboratory for Light-Weight Materials, Nanjing Tech University, Nanjing 211816, China
[d] Department of Mechanics, School of Aerospace Engineering, Huazhong University of Science and Technology, Wuhan 430074, China
[e] Mateis, INSA Lyon, Université de Lyon, Villeurbanne F-69621, France
[f] ESRF - The European Synchrotron, Grenoble 38043, France

ARTICLE INFO

Article history:
Received 23 December 2021
Revised 17 July 2022
Accepted 2 August 2022
Available online 3 August 2022

Keywords:
Self-healing
Aluminum alloys
Synchrotron radiation computed tomography
In situ TEM
In situ tensile test

ABSTRACT

Self-healing strategies aim at avoiding part repair or even replacement, which is time consuming, expensive and generates waste. However, strategies for metallic systems are still under-developed and solid-state solutions for room temperature service are limited to nano-scale damage repair. Here we propose a new healing strategy of micron-sized damage requiring only short and low temperature heating. This new strategy is based on damage localization particles, which can be healed by fast diffusing atoms of the matrix activated during heat treatment. The healing concept was successfully validated with a commercial aluminum alloy and manufactured by Friction Stir Processing (FSP). Damage was demonstrated to initiate on particles that were added to the matrix during material processing. *In situ* 2D and 3D nano-imaging confirmed healing of the damaged material and showed that heating this material for 10 min at 400°C is sufficient to heal incipient damage with complete filling of 70% of all damage (and up to 90% when their initial size is below 0.2 µm). Furthermore, strength is retained and the work of fracture of the alloy is improved by about 40% after healing. The proposed Programmed Damage and Repair healing strategy could be extended to other metal based systems presenting precipitation.

1. Introduction

Aluminum alloys have many applications in aerospace or transportation industry, where the strength-to-weight ratio should be maximized [1–3]. However, the relatively low damage tolerance of high strength Al alloys remains a major challenge for increasing product lifetime [3,4]. During service, parts might accumulate damage requiring repair or even replacement, which is time consuming, expensive and generates waste. Now, aluminum alloys are facing one limitation intrinsic to metallic materials: once damage has initiated, it will not vanish [5]!

Self-healing (SH) materials are able to suppress initiated damage [5–9]. This strategy brings about a new paradigm in materials design and is already well-developed for polymers, cement, asphalt, and ceramics, but under-exploited for metallic materials [5,6,9]. The general difficulty with SH metallic systems is the low mobility of atoms at room temperature and often the need for an external driving force to promote mass transfer, without sacrificing the strength of the system [5–10].

Several strategies are currently under development for SH metal-based systems which were categorized by Grabowski and Tasan depending on the dimension of the healed damage [6]. Strategies in systems where millimeter-scale cracks can be healed are based on electro-healing (e.g. for steels and Ti alloys) [11,12] or liquid-based systems based on melting of one component of the system (e.g. low melting point Sn-Bi phase) filling the cracks [5–8,13]. Both systems correspond to a group of assisted healing, where the electro-healing group needs external electrical field and the other one needs external heat [5].

Electro-healing is a recently developed and promising strategy for steels, Ni and Ti alloys, that can be divided into two groups: electro-healing inside electrolyte solution and electropulsing treatment without electrolyte solution [14]. One advantage of these strategies is that they do not require any alloy microstructural modifications. However, the use of electrolyte solution is a practical limitation and no results are available for Al alloys. More details on these healing strategies can be found elsewhere [5,6,14].

* Corresponding author.
E-mail address: aude.simar@uclouvain.be (A. Simar).

https://doi.org/10.1016/j.actamat.2022.118241
1359-6454/

Liquid-based systems can be divided into three groups: the ones using solder tubes or capsules containing healing agent, the ones using coating as a healing agent and the ones using low melting point eutectics (also exploiting shape memory alloys) [14]. However, their applicability is limited by the requirement to maintain the shape of the part, prevent liquid leakage and solidification cracking during the healing cycle [5,7]. Furthermore, these materials have limited potential for structural components due to their low mechanical properties and their high anisotropy [5,6].

Another SH strategy in metals is based on the solid-state diffusion of a healing agent leading to precipitation inside nano- and micro-scale voids of a new phase [5,6,15]. This healing strategy requires the availability of atoms in solid-solution in supersaturated state and their mobility and is thus only applicable for selected alloys. Common systems here are precipitation hardenable Al alloys in underaged state where alloying elements are in supersaturated solid solution offering healing potential as presented in Refs. [16,17]. Underaged Al alloys are in low strength state, presenting less interest for applications requiring high strength. Current solid-state precipitation-based healing metals can be divided into two categories depending on external trigger used to promote diffusion: Thermally activated Diffusion and Precipitation (TDP) and Pipe Diffusion and Precipitation (PDP), see Fig. 1a.

Thermally activated Diffusion and Precipitation TDP (Fig. 1a,b) is facilitated by (i) nanoscale cavities formed at grain boundaries, (ii) relatively high homologous temperatures (Fig. 1b) and (iii) relatively long service time, all typical of creep damage [15,18]. One major difficulty associated with TDP is that the healing precipitation happens not only at the damaged area but also throughout the microstructure, reducing the number of super-saturated solute atoms available in the matrix for healing [6,18].

Pipe Diffusion and Precipitation PDP (Fig. 1a,b) falls within the low-temperature applicability window where diffusion is very slow for transport of solute elements to damage sites. This is typical of long fatigue loadings during which microplasticity generates regions of vacancies and high dislocation densities where damage is more likely to nucleate due to dislocation pile-ups [6]. Precipitation takes place in these regions due to pipe diffusion, i.e. diffusion of solute elements along dislocations. PDP demonstrated improved fatigue resistance in commercial Al-Cu-Mg alloys in underaged state compared to peak-aged state [17,19]. Limitations of PDP are (i) the capacity to only heal nanoscale damage (Fig. 1c) and (ii) environmental effects to the near-surface cracks hindering crack healing [5,6,20].

2. A new healing strategy: programmed damage and repair

Here, we propose a new solid-state healing strategy called *Programmed Damage and Repair* (PDR, Fig. 1a, bottom) applied to an Al alloy. It incorporates damage localization particles within a commercial Al alloy. Damage primarily nucleates on these particles (hence *Programmed Damage*) modifying the common void nucleation mechanism in Al alloys, i.e. by fracture or decohesion of iron-rich intermetallics [21,22]. During service, loading is interrupted and a healing heat treatment (HHT) triggers diffusion to heal these voids (hence *Repair*). Temperature and time are selected to minimize microstructural changes that would lead to strength decrease, keeping a reasonable healing efficiency.

Our new PDR strategy presents a notable difference to the two strategies discussed above. While the TDP and PDP (Fig. 1a) concepts use precipitation event at nano-voids as healing mechanism, the PDR strategy is based on fully precipitated microstructure where these precipitates play the role of “damage localization particles”. The second difference relates to the healing mechanism. In our new concept, the matrix itself is the healing source, not for precipitation as our microstructure is already fully precipitated, but for matrix penetration into the crack by exploiting fast atomic diffusion mechanisms.

This PDR strategy presents several advantages compared to TDP and PDP. In particular, although PDR requires thermal activation like TDP, the material is heated for only a limited time (Fig. 1c, top) at temperatures slightly above the upper limit of TDP strategy to ensure sufficient diffusion. Furthermore, PDR is not restricted to healing nanoscale damage contrary to PDP (Fig. 1b), i.e. PDR repairs damage at a scale controlled by the damage localization particles. Moreover, in the TDP and PDP strategies, precipitation is difficult to control and leads to a reduction in healing efficiency [6,18]. The PDR strategy relies on strengthening and particles that strengthen the alloy and also serve as well-controlled damage sites and healing agent concentrators. The healing efficiency is thus expected to be maintained for multiple healing cycles (Fig. 1c, bottom).

In addition, healing potential can be enhanced by a high density of crystallographic defects such as vacancies, dislocations, subgrain and grain boundaries and eventually internal surfaces (i.e. the surfaces of the induced voids). Such defects provide diffusion shortcuts and thus increase diffusion rates. Processing methods that can achieve such microstructures can thus enhance the material’s healing potential [23,24].

3. Experimental methods

3.1. Manufacturing

To obtain the desired microstructure, Friction Stir Processing (FSP) was applied on commercial Al 6063 alloy, a representative alloy of the Al-Mg-Si system. FSP is a well-known technique for ductility and strength improvement of aluminum alloys as well as for particles incorporation to obtain Aluminum based Matrix Composites (AMCs) [2,25,26]. FSP leads to refinement and homogenization of the microstructure and the processed material typically contains a high amount of crystal defects, i.e. vacancies, dislocations, subgrain and grain boundaries. These microstructural features provide, on the one hand, nucleation sites for precipitation and, on the other hand, increasing healing potential by the presence of diffusion shortcuts for fast-diffusing atoms [14,24].

Friction Stir Processing (FSP) was applied on an Al6063-T4 plate ($300 \times 70 \times 5$ mm) (see Supplementary material 1). To introduce the damage localization particles, a $240 \times 5 \times 0.5$ mm^3 groove was machined in the middle of the plate and filled with a 99.9% purity Mg strip of the same geometry, covered by a 1 mm thick cold rolled 6063 plate. FSP was conducted on a FSW machine E256 (TRA-C Industry), using a H13 steel tool. The FSP tool has a 20 mm diameter shoulder, a 5.6 mm diameter and 2 mm long pin, penetrating 2.2 mm into the plate. Sixteen passes of FSP were performed with a rotational speed of 1000 rpm and a traverse speed of 400 mm/min in order to ensure good distribution of Mg.

3.2. Alloy composition and conventional microstructure observations

Chemical analysis was conducted by Inductively Coupled Plasma (ICP) - Atomic Emission Spectroscopy (AES) on a iCAP 6000 equipment (Thermo Scientific). Microstructural characterization was performed using Scanning Electron Microscopy (SEM, Zeiss ultra 55). Further investigations on damage localization particles, their chemical composition and the composition of the matrix were performed with FEI Osiris Transmission Electron Microscope (TEM) operated at 200kV and equipped with a CHEMISTEM detector. Samples were prepared from the top surface of the nugget zone at a depth of at least 0.5 mm. TEM thin foils were prepared by soft ion milling (Gatan Duo Mill 600 machine).

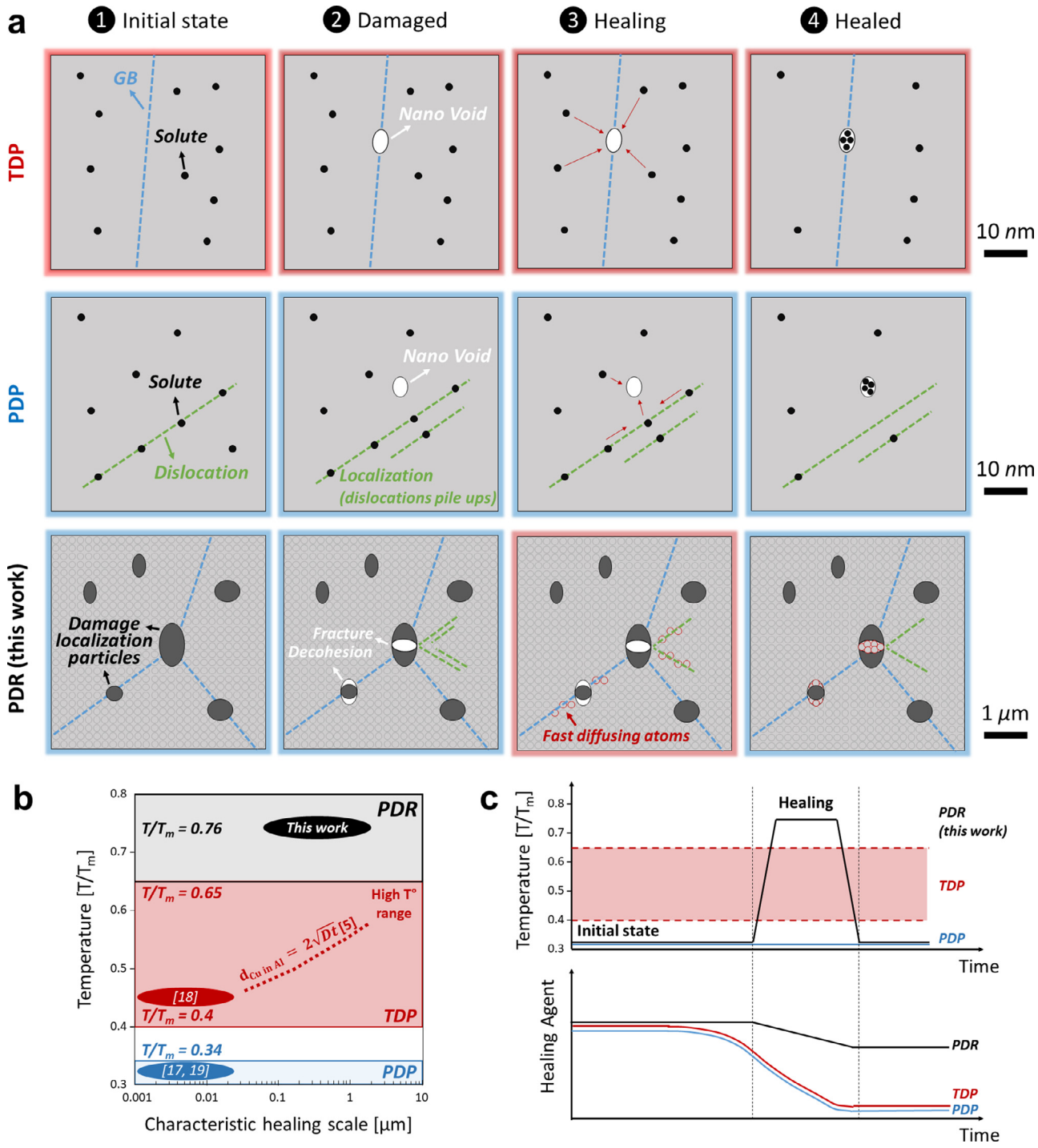

Fig. 1. Healing strategies in metallic materials. (a) Schematic overview of solid-state self-healing strategies in metals inspired from Grabowski and Tasan [6] (TDP = Thermally activated Diffusion and Precipitation, PDP = Pipe Diffusion and Precipitation and PDR = Programmed Damage and Repair). (b) T/T_m – homologous temperature as a function of characteristic healing scale (temperature (in K), T_m – melting temperature (in K)). Temperatures below $T/T_m \approx 0.34$ (in blue) correspond to the PDP strategy operating at room temperature. The "High T° range" (in red) corresponds to TDP strategy and is inspired from [5]. The limits are defined as upper and lower operation limits for creep-loaded samples. The red doted line corresponds to the calculated theoretical healable damage size evolution with temperature assuming a characteristic diffusion length of Cu in pure Al after 10^5 seconds. The PDR strategy points are placed at 400°C ($T/T_m \approx 0.76$), see Section 4.3. Numbers [17,19] and [18] in the figure refer to the corresponding papers in the reference list. (c) Evolution of homologous temperature and healing agent concentration with time for these strategies.

3.3. In situ *SEM tensile test*

To reveal damage mechanisms, *in situ* uniaxial tensile tests were performed inside the SEM using a micro-tensile machine (Gatan microtest tensile stage). Void formation and coalescence could thus be monitored. Flat samples with a thickness of 1 mm were extracted from the top part of the FSPed plate (see Supplementary material 1). The detailed geometry of these samples is provided in Fig. 2a. The loading rate was set to 0.1 mm/min. To force the crack initiation site and facilitate observations, the flat tensile samples contained U-shaped notches on both sides (Fig. 2a).

These *in-situ* tensile tests have been interrupted at elongations of 0.6 mm or 0.7 mm. These two levels of elongation have been

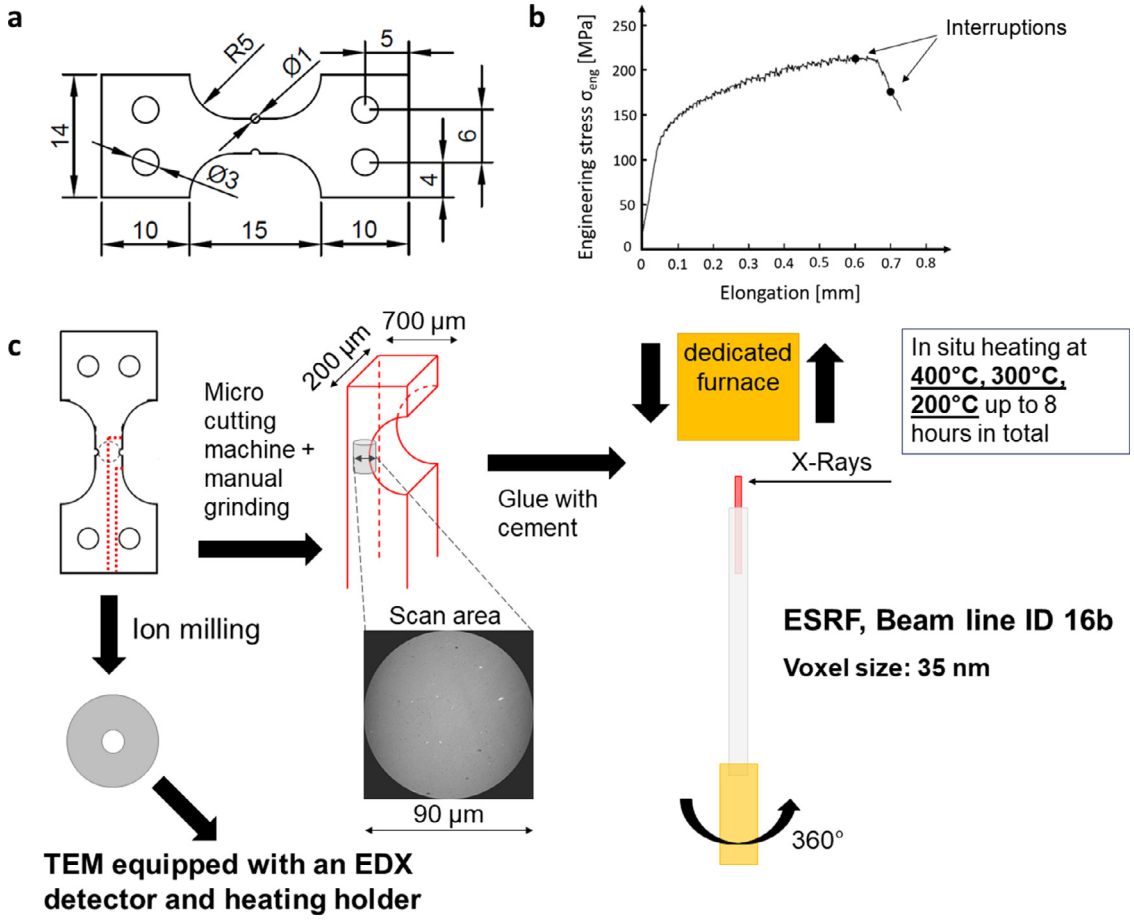

Fig. 2. Samples preparation for *in situ* SEM tensile testing, *in situ* TEM heating and *in situ* 3D X-Ray nano-imaging. (a) Geometry of *in situ* SEM tensile test sample (thickness about 1 mm); (b) Representative interrupted engineering stress-strain curve at 0.6 or 0.7 mm elongation in comparison with a curve where the test was performed without observation and until fracture; (c) Steps of sample preparation and schematic for *in situ* 3D X-Ray nano-imaging and *in situ* TEM heating experiments.

selected in order to ensure a significant number of voids nucleated from the reinforcement particles.

In order to estimate more precisely the applied strain in the sub-specimen (extracted for *in situ* 3D X-Ray nano-imaging using holotomography) at the notch root (see Fig. 2c), finite element (FE) analysis of the SEM tensile tests was performed (see Fig. 3). The input file of this model was constructed and solved with the general-purpose software ABAQUS (version 2019). Young's modulus and hardening law were identified from the experimental macroscopic stress-strain curves of uniaxial tensile tests (Section 3.6). Isotropic hardening was assumed and 3D linear hexahedral elements (C3D8R) were used. The FE procedures are fully standard and convergence of the results was carefully checked (with 16 elements in the thickness direction).

Fig. 3 shows both the experimental and computed force-displacement curves of the SEM tensile tests. A good agreement is observed up to elongation value of approximately 0.75 mm. Fig. 3c, d shows contour plots of von Mises equivalent strain within a cross-section through the center of the notch for an elongation of 0.6 and 0.7 mm, respectively. The strain levels within the tomography specimens (Fig. 3b–d) range between [0.3–0.45] and [0.4–0.6] for the elongation of 0.6 mm and 0.7 mm, respectively.

3.4. In situ *X-Ray synchrotron holotomography heating*

The *in situ* 3D X-Ray nano-imaging tests were performed at the European Synchrotron Radiation Facility (ESRF, Grenoble, France) on beamline ID16B using holotomography with a voxel size of 35 nm and a dedicated high temperature furnace [27–29]. All 3D X-Ray nano-imaging specimens were prepared according to the schematic in Fig. 2c. The specimens were thus taken from interrupted *in situ* SEM tensile tests at 0.6 mm and 0.7 mm of global elongation (corresponding to a strain level of about 0.35 and 0.5, respectively, see Section 3.3). They were extracted next to the notch, i.e. in the region experiencing the largest strain and thus presenting the highest level of damage (Fig. 2c). The samples were then thinned manually to 200 µm and cut by a micro-cutting machine. The specimens were mounted on a dedicated specimen support (Fig. 2c) to fit into the furnace available at the beamline [27]. The furnace can be easily mounted and removed over the specimens to heat them up to 200, 300 and 400°C between holotomography scans without moving the specimens. The nano-imaging were acquired using a conic pink beam ($\Delta E/E$=10-2) with an energy of 17.5 keV. While the specimen rotated over 360°, 2D phase contrast images of the specimen (field of view: 90 × 76 μm^2 – pixel size: 35 nm) were recorded using a CMOS camera. For each tomographic scan, 3009 projections were acquired with an exposure time of 200 ms per step.

For selected scanning steps, cavities were distinguished from the Al matrix by segmentation and their geometrical characteristics were recorded. A tracking algorithm (in-house built toolbox in MATLAB), relying on a graph-based data association approach, has been modified and used to follow the cavities from one scanning step to the next (see Supplementary material 5 for details of the procedure) [30,31]. Only the cavities with initial size above 0.1 µm (i.e. with a diameter of at least 3 voxels) were used for the tracking procedure in order to avoid counting any noise of the re-

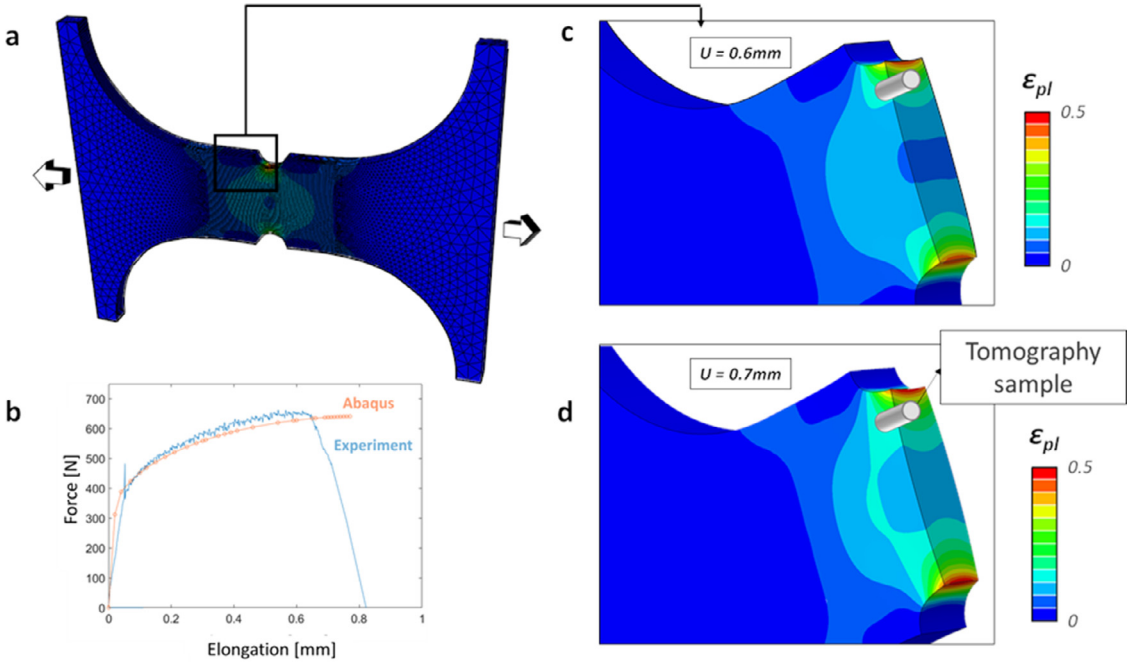

Fig. 3. Finite element analysis of SEM tensile samples. (a) Finite element mesh of the whole specimen; (b) Experimental and computed Force-displacement curves of the SEM tensile tests. Contour plots of von Mises equivalent strain within a cross-section through the center of the notch for an elongation of (c) 0.6 and (d) 0.7 mm.

constructed images. The results of the tracking algorithm allow to perform a statistical analysis of void healing, i.e. voids which have completely disappeared.

Supplementary material 2 provides a detailed list of all samples with the elongation used before 3D X-Ray nano-imaging, the healing temperatures and times. Reference samples without adding the Mg strip were also manufactured to assess the influence of magnesium addition on the healing potential. The results of these additional specimens are provided in Supplementary material 4.

3.5. In situ *TEM heating*

TEM was used for *in situ* heating also using the FEI Osiris TEM operated at 200kV. The TEM specimens were also prepared from interrupted *in situ* SEM tensile test at a global elongation of 0.6 mm by analogy with the specimens for 3D X-Ray nano-imaging (Fig. 2c), then also thinned using ion-milling. A Gatan 652 double-tilt heating holder was used for the *in situ* TEM heating experiments. To assess the healing mechanism, the optimum temperature of 400°C (see Section 4.3) was used with heating interruption for observation. The heating time from room temperature (RT) to 400°C was less than 1 min. All images were taken in HAADF-STEM mode to facilitate the observation of the particles and cracks.

3.6. *Micro-hardness and uniaxial tensile test*

Vickers micro-hardness testing was performed along the FSP nugget zone with a EMCO-test DuraScan G5 indentor under 0.3 kg loading (HV0.3). Uniaxial tensile tests were performed on a screw-driven universal machine under displacement control with 0.5 mm/min velocity. Flat samples, with a cross-section of 2 × 6 mm^2, were machined along the FSP direction (Supplementary material 1 and 7). The initial gauge length was equal to 22 mm. The true fracture stress (defined as $\sigma_f = F_f/A_f$) and the true fracture strain (defined as $\varepsilon_f = \ln(A_0/A_f)$) were computed from the last force value F_f recorded before fracture, and from the initial and fractured section area, A_0 and A_f, respectively. In order to identify the work of fracture (W_f), the area under true stress-strain curves was calculated. The samples Al-0.5Mg_2Si-HHT were strained to 10, 15, 18 and 20% (i.e. UTS reached) of global elongation before the healing heat treatment (HHT) was applied. The heat treatment was performed at 400°C using Heraeus heating oven by the placement of flat samples in contact with the heating plate and subsequent cooling in air.

4. Results and discussion

4.1. *Initial and damaged microstructure characterization*

After FSP with an embedded Mg strip, inductively coupled plasma (ICP) analysis shows that the overall Mg content was increased by 3% (from 0.4 to 3.4 wt.%) (Supplementary material 1, Table S1). Fig. 4a, b show that the new alloy consists of an Al matrix rich in Mg, containing about 0.5% surface fraction of Mg_2Si particles (in dark grey) and brittle Fe-rich intermetallics (in white), which are always present in industrial aluminum alloys and are source of damage as was shown by Hannard et al. [22]. Supplementary material 1 provides a quantitative characterization of these Mg_2Si particles.

Homogeneously distributed 300 nm size Mg_2Si particles (Fig. 4a) are formed *in situ*, modifying the microstructure of Al6063 alloy and providing hardening effect. Selected area electron diffraction pattern (SAED) in Fig. 4e confirms that this phase is Mg_2Si. The hardness of the nugget zone is increased from 52.36±0.94 for Al6063-FSP to 76.31±1.3 HV0.3 (see Supplementary material 1, Fig. S2 for full hardness map).

Fallah et al. [32] have shown that Mg enrichment in the matrix favors an early stage Mg-Si clusters nucleation, stabilization and growth. These early stage clusters can easily be transformed to an equilibrium Mg_2Si phase [33]. Fig. 4d–f shows that the Si content is almost entirely used for Mg_2Si precipitation (Fig. 4d–f), while 3 wt.% Mg remains available in the matrix (Fig. 4f) for further healing. These results of the phases compositions correspond well to the ones obtained by Thermo-Calc simulation for the same composition identified by ICP analysis (Supplementary material 1, Table S2) at the expected FSP temperature of 490°C (≈ 0.8 T_m). This

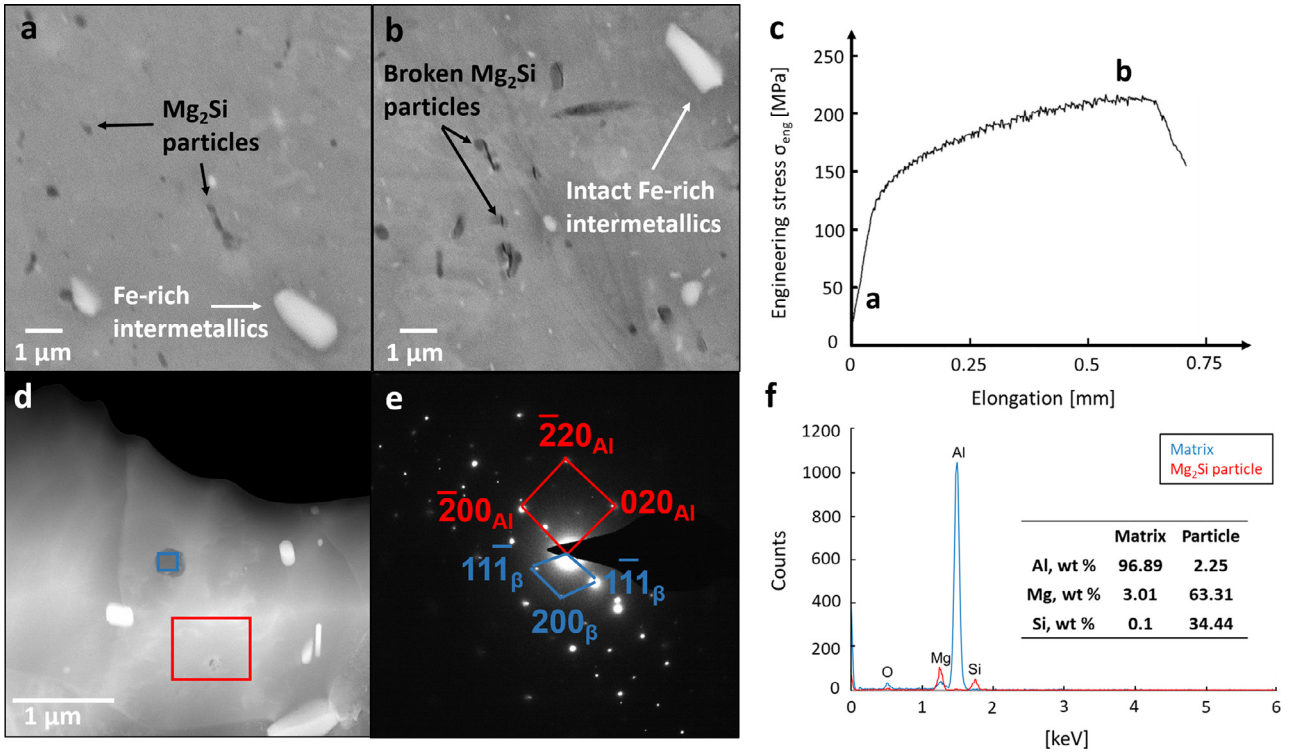

Fig. 4. Microstructure and damage evolution in Al6063-0.5Mg_2Si alloy. (a) Al6063-0.5Mg_2Si microstructure: in dark grey – Mg_2Si particles; in white – Fe-rich intermetallics; (b) damage nucleated on Mg_2Si particles at 0.6 mm of global elongation; (c) tensile curve obtained during *in situ* scanning electron microscopy tensile test indicating the elongations corresponding to (a) and (b); (d) HAADF-STEM (high-angle annular dark-field scanning transmission electron microscopy) micrograph; (e) SAED (Selected Area Electron Diffraction) pattern obtained on a particle and the surrounding matrix; (f) EDX (Energy Dispersive X-Ray Analysis) analysis of a particle (blue box) and surrounding matrix (red box) indicated in (d). Both SAED and EDX confirm that these particles are Mg_2Si.

means that the cooling rate after FSP was high enough to form a supersaturated solid solution rich in Mg.

Both Mg_2Si particles and Mg enrichment of the Al matrix are important for the PDR strategy: the Mg_2Si precipitates serve as damage sites and therefore generate Programmed Damage, while the high diffusion rate of Mg in the Al matrix are expected to speed up void healing (i.e. Repair) [10].

Fig. 4b shows that damage initiates on Mg_2Si particles by their fracture or debonding from the matrix only after significant tensile deformation during *in situ* SEM tensile testing (Fig. 4c), similar to Shen et al [34]. Fe-rich intermetallics remain generally intact until final fracture, enabling large deformation range for healing before catastrophic failure, i.e. void nucleation on brittle Fe-rich intermetallics in the matrix is effectively replaced by the programmed damage at damage localization particles (for a proof with *in-situ* SEM tensile tests see Supplementary material 3).

This new alloy indeed presents novel microstructural features compared to previous solid-state SH metallic systems:

(i) small (below 1 µm) homogeneously distributed Mg_2Si particles are controlled damage sites limiting initial damage size;
(ii) enrichment of the Al matrix in Mg atoms speeds up solid-state diffusion at temperatures below homogenization while Al can also serve as healing agent [10];
(iii) since the matrix serves as a healing agent reservoir, the delivery of healing agents is continuous during applied HHT expectedly ensuring multiple healing cycles (Fig. 1c) [35];
(iv) the "damage localization particles" present a strengthening effect as opposed to the underaged aluminum alloys (see introduction, PDP) [16,17].

In addition, a commercial 6063Al alloy is used as base material instead of alloys developed with specific compositions for SH purpose or high purity metallic systems [15,36]. Finally, FSP improves the ductility of the matrix material by up to 100% by microstructure homogenization and refinement, and eliminates the need for any post-treatments [2,37,38].

4.3. Selection of the healing temperature

3D X-ray nano-imaging was performed at the ESRF (see Supplementary material 2 for sample full list). Three temperatures were selected to investigate the healing efficiency: 200, 300, and 400°C, which correspond to values T/T_m = 0.54, 0.65 and 0.76, with the melting temperature of Al 6063 alloy taken as 610°C or 883 K. These values are expected to be sufficient to activate fast diffusing atoms. Fig. 5 presents microstructural evolutions for healing at 200°C and 300°C.

It is observed that for the 200°C heating temperature (Fig. 5a), even 8 h are not sufficient to cause healing and most voids remain unaffected. Similarly, 100 min at 300°C are not sufficient to show significant healing (Fig. 5b). Although the healing of the voids is more prominent at 300°C, it still cannot be considered sufficient in comparison with a healing temperature of 400°C (Fig. 6). Thus, in what follows, 400°C will be selected as healing temperature and the relevant temperature range of PDR is placed in Fig. 1(b,c).

4.2. Statistical validation of healing ability

Correlative characterization over time was used to analyze healing ability [39]. Fig. 6a shows the disappearance and progressive filling of larger voids observed during *in situ* HHT coupled to 3D X-ray nano-imaging performed at the selected temperature of 400°C. Fig. 6b shows the results of the tracking algorithm used to follow the progressive filling of each individual void from one 3D scan to

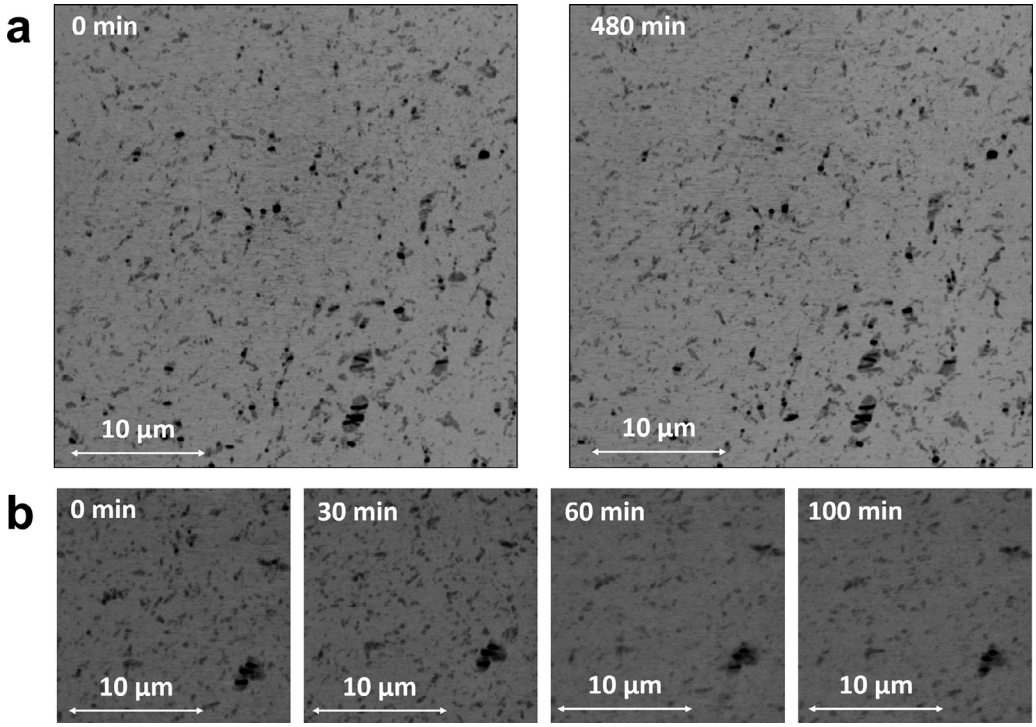

Fig. 5. Minimum Intensity Projections (MinIP) of 50 slices of volumes obtained before and after heat treatment (a) up to 8 h at 200°C and (b) and up to 100 min at 300°C using X-ray holotomography. These specimens correspond, respectively, to Specimen 4 and 5 of Supplementary material 2.

the next. A clear size effect is observed: the smallest cavities (below 200 nm) have a healing efficiency of approximately 90% after 10 min, while the largest cavities (larger than 400 nm) present a much lower healing efficiency (20%). Further heating shows continuous healing of voids regardless of their size or deformation level at which HHT is performed. After 2 h, approximately 85% of all nucleated voids are completely filled and the biggest healed void is about 2 µm in length (Fig. 6a).

Fig. 6c shows the cumulative distribution function of the near-neighbor distance (NND) of each void just after damage (initial state) and after various HHT durations. It shows that a lot of voids have at least one neighbor in very close proximity in the initial state (i.e. small NND), while voids become distant from each other after HHT (i.e. larger NND). For example, while all voids have a NND below 4 μm in the initial state, only 60% of voids have a neighbor located at less than 4 μm after 10 min of HHT (Fig. 6c). Healing postpones thus failure as only closely spaced voids are likely to merge to form micro-cracks.[22] Fig. 6d shows that the void volume fraction is already significantly decreased after 10 min of HHT. Clearly 10 min HHT is thus sufficient to significantly decrease both the number of voids close to each other and the volume fraction of voids.

4.3. Healing mechanism

Fig. 6e shows results of *in situ* heating in the transmission electron microscope at 400 °C with a typical example of healing mechanism (more results are provided in Supplementary material 6). The healing shown in Fig. 6 can be interpreted by analogy with metal sintering, where the driving force of initial porosity closure is the decrease in interfacial energy, achieved by a reduction in free surface area per unit volume [5,40]. Thermal activation is required to trigger diffusion and start voids filling (by analogy with densification during sintering). At elevated temperature, diffusion is enhanced and oriented following the chemical potential gradient issued from concentration gradient: atoms will diffuse from areas presenting high concentration towards areas with lower concentration.

By analogy with sintering, a sharp crack tip can be considered as a void with a very low dihedral angle. Low dihedral angles promote densification, favoring crack filling (Fig. 6e) [41]. The developed Al-0.5Mg_2Si alloy facilitates this process in three ways, which expectedly work in parallel.

(i) FSP generates high density of defects as vacancies, dislocations and grain boundaries, as well as a very fine distribution of Mg_2Si particles mainly forming at grain boundaries (Supplementary material 6) [26]. Broken particles are thus connected to these diffusion “shortcuts” and grain boundary diffusion of Al and Mg atoms can easily be activated [24].

(ii) The region in front of the crack tip presents high stress concentration and higher dislocation density providing a favorable path for pipe diffusion [24].

(iii) While an increase of Mg atoms concentration was not detected in the area of a healed crack (Supplementary material 6, Fig. S10), the supersaturated solid solution of Mg atoms within the Al matrix (about 3%, Fig. 4d,f) is expected to play a significant role in healing kinetics and also contributes to the two factors discussed above [10]. Mg atoms have a higher diffusion rate in the Al matrix than Al self-diffusion [10]. The solubility of Mg in the Al matrix is below 1% at room temperature and Mg should remain as super-saturated atoms or gather in Al-Mg rich GP zones [42,43]. The 400°C HHT increases the solubility of Mg in Al to about 13% leading to a release of all trapped Mg atoms from the clusters to the matrix for diffusion and healing [44]. Mg atoms are neighboring and accompanying vacancies and dislocations because of steric effects [45,46]. Heating will activate the migration of a flux of defects towards grain boundaries acting as a sink [45,47]. Thus, Mg atoms trapped at these defects will diffuse from the matrix to the grain boundary where they can further travel along the grain boundary towards the crack (Fig. 1a). Now the question is how can vacan-

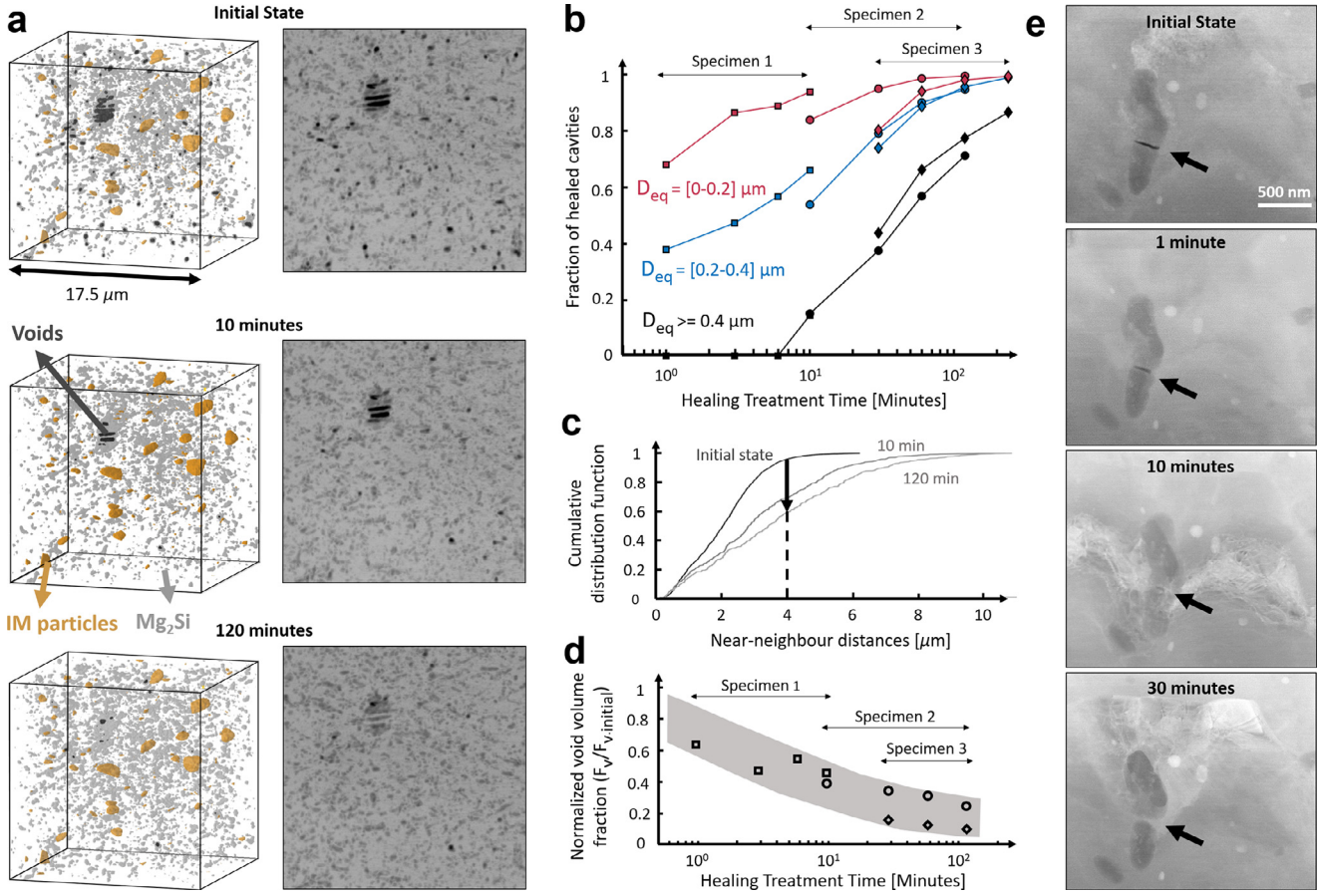

Fig. 6. Healing evolution with time at 400°C. (a) 3D volumes and corresponding Minimum Intensity Projections (MinIP) in the initial state, after 10 min and after 2 h at 400 °C; (voids are in black, intermetallic particles in yellow and Mg_2Si particles in grey). (b) Evolution of the number of healed cavities with healing time for different size classes: Specimens 1 and 2 correspond to 0.6 mm of global elongation; Specimen 3 corresponds to 0.7 mm of global elongation (see Supplementary material 2 for details on each specimen). (c) Cumulative distribution function (CDF) of the near-neighbour distances between voids as a function of the heating time. (d) Evolution of the void volume fraction (F_v), normalised by the value in the initial state ($F_{v,init}$). (e) HAADF-STEM images showing healing evolution with time. The black arrows indicate the position of the crack.

Table 1
Mean values for tensile properties of the composite samples before and after the healing heat treatments.

	E[a)] [GPa]	σ_y [MPa]	σ_y[b)] [MPa]	$\sigma_{Failure}$[c)] [MPa]	ε_f	W_f[b)] [MJ/m^3]	W_f [MJ/m^3]
Al-0.5Mg_2Si	69.3±1.2	124.8±3.1		394.73±10.7	0.65±0.1		196.3±15.3
Al-0.5Mg_2Si-HT	67.1±0.8	131.5±3.0		416.90±29.6	0.76±0.00		236.6±23.5
Al-0.5Mg_2Si-HTT	67.0±3.8	125.7±4.2	175.6±9.3	428.9±32.8	0.74±0.03	242.5±12.1	273.7±16.8

[a)] E – Young modulus
[b)] data for Post Healing Loading curve
[c)] $\sigma_{Failure}$ – Strength at failure

cies annihilate? By analogy with the final stage of sintering, grain boundaries can act as healing atoms source as well as vacancies sink [40,48].

In order to confirm the unique healing behavior of the proposed healable alloy and indirectly verify the importance of Mg enrichment, the same commercial alloy Al6063 was processed under the same condition but without Mg strip addition. In that case, the same healing phenomenon was not observed (Fig. S5 of Supplementary material 4).

4.4. Effect of healing treatment on tensile properties

To evaluate the effect of healing efficiency on mechanical properties, another kind of tensile tests was performed (Supplementary material 7) on three Al-0.5Mg_2Si alloys (Fig. 7a, Table 1):

(1) as-FSPed (called Al-0.5Mg_2Si);
(2) non-damaged but heat treated at 400°C for 10 min (called Al-0.5Mg2Si-HT);
(3) damaged by loading to deformation levels up to 20% (details in Supplementary material 7), heat treated then loaded until final failure (called Al-0.5Mg_2Si-HHT).

Heat treating the undamaged alloy improves the fracture strain ε_f from 0.65±0.06 (Al-0.5Mg_2Si) to 0.76±0.05 (Al-0.5Mg_2Si-HT) without significantly affecting yield strength (σ_y) (Fig. 7a, Table 1) likely due to static recovery of the FSPed microstructure [49].

Al-0.5Mg_2Si-HHT was deformed up to strain close to the onset of plastic localization. At this stage, particles are fractured (Fig. 4b), and if no healing is applied before further deformation, voids will grow, coalesce into macrocracks leading to catastrophic failure. However, damage is significantly decreased by applying HHT. Al-

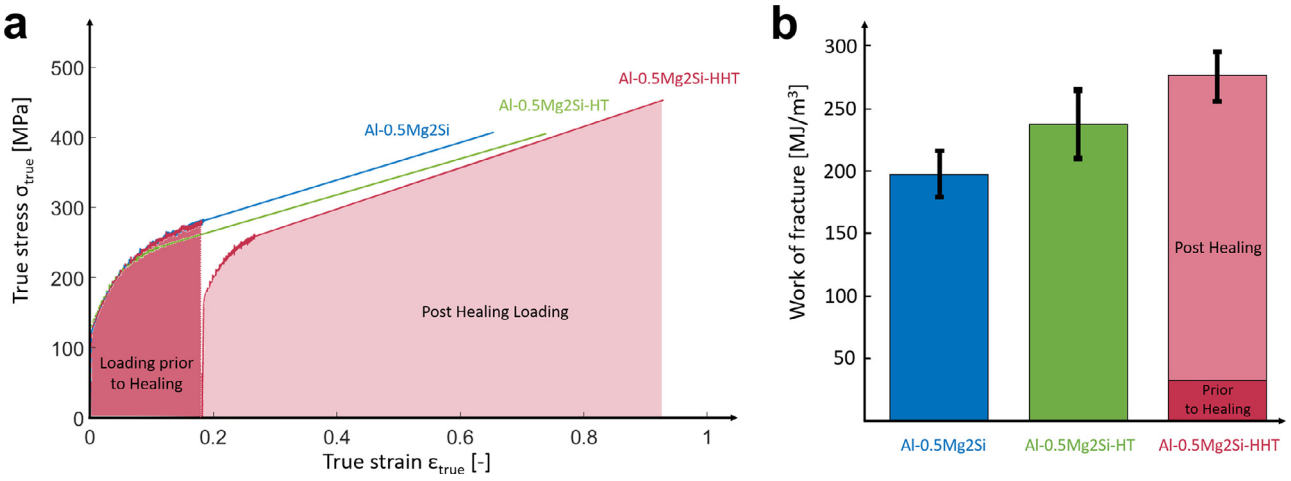

Fig. 7. Mechanical behavior of Al-0.5Mg_2Si samples. (a) Typical true stress-strain curves of the Al-0.5Mg_2Si samples; (b) corresponding work of fracture.

0.5Mg_2Si-HHT presents a similar fracture strain to Al-0.5Mg_2Si-HT: 0.74±0.03 (or 0.90±0.07 taking into account the deformation applied before healing).

The work of fracture (W_f) quantifies the amount of energy that the material can absorb before failure, evaluated from the area under the true stress-strain curves (Fig. 7a), and is used as an indicator of fracture toughness [38,50]. Fig. 7b shows that healing recovers the work of fracture of the damaged but post-healed sample (considering only the "Post Healing" cycle) to a level similar to the Al-0.5Mg_2Si-HT sound sample. In addition, the total work of fracture of the healed Al-0.5Mg_2Si-HHT sample (including both loading "Prior to Healing" and "Post Healing" cycles) is 40% above that of Al-0.5Mg_2Si (Fig. 7b, Supplementary material 7, Table S5).

An overall analysis of the curve indicated as "Post Healing Loading" in Fig. 7a shows that the material after HHT does not present any yield stress, ultimate tensile stress, fracture strain nor work of fracture loses compared to Al-0.5Mg_2Si-HT and in this perspective behaves like undamaged material even though it underwent the "Loading prior to Healing" cycle generating damage.

One should note that recovery, recrystallization and in general heat treatment softening mechanisms also play a role on the tensile behavior after the HHT. Now, compare samples Al-0.5Mg_2Si-HHT and Al-0.5Mg_2Si-HT (Fig. 7b). The 16% improved W_f with the same heat treatment (including both loading "Prior to Healing" and "Post Healing" cycles), i.e. expectedly leading to a similar softening, brings the conclusion that damage healing contributes to W_f of the healed sample (Al-0.5Mg_2Si-HHT). Indeed, voids (i.e. small cracks) closure causes a reduction in NND (Fig. 6c). For neighboring damage to coalesce, regions of elevated strain (the regions in front of the crack tips) should overlap. The HHT increases the distance between voids and thus postpones void coalescence.

5. Conclusion and outlook

This work presents a new precipitation-based healing strategy for metals. A proof of concept using commercial Al alloy shows that one healing cycle fully recovers mechanical properties and overall improves work of fracture by 40% compared to the initial state of the material. The proposed Programmed Damage and Repair (PDR) strategy overcomes many reported limitations for self-healing (or healable) Al-based alloys particularly taking a step forward from nanoscale damage healing to a few microns scale. Further development of PDR strategy achieving full healing is expected to lead to multi-cycle healable alloy. Moreover, as FSP can be applied locally or like a surface treatment in commercial Al alloys, these new healable alloys could enhance local areas of stress concentrations, granting prolonged service life to structures.

Although not investigated yet, we anticipate that our concept could expand to other alloys with a precipitation phenomenon (e.g., 7xxx Al alloys, Mg alloys). As a result, the PDR strategy has great potential to impact the classical paradigm in metallic materials design, where only damage delay and prevention are considered as optimization routes. In addition, the proposed strategy can be adopted by other processes where two conditions meet: possibility to modify chemical composition in order to obtain damage localization particles and supersaturated solid solution; and possibility to control processing conditions so fine microstructures presenting diffusion shortcuts can be produced and well-controlled, e.g., additive manufacturing.

Declaration of Competing Interest

The authors declare that they have no known competing financial interests or personal relationships that could have appeared to influence the work reported in this paper.

Acknowledgements

This work was supported by the European Research Council for a starting grant [grant agreement - 716678], the Belgian National Fund for Scientific Research – FNRS, Belgium [Grant CDR – J.0113.20, FRIA grant - 35484217] and the ESRF for provision of radiation facilities [proposal MA-4353]. F.H. acknowledges the Belgian National Fund for Scientific Research (FNRS) for his postdoctoral fellowship at UCLouvain. H. Idrissi is mandated by the Belgian National Fund for Scientific Research (FSR-FNRS).

Supplementary materials

Supplementary material associated with this article can be found, in the online version, at doi:10.1016/j.actamat.2022.118241.

References

[1] I. Polmear, D. StJohn, J.F. Nie, M. Qian, Light Alloys: Metallurgy of the Light Metals, 5th ed., Butterworth-Heinemann, 2017, doi:10.1016/b978-0-08-099431-4.00010-5.
[2] F. Hannard, S. Castin, E. Maire, R. Mokso, T. Pardoen, A. Simar, Ductilization of aluminium alloy 6056 by friction stir processing, Acta Mater. 130 (2017) 121–136, doi:10.1016/j.actamat.2017.01.047.
[3] N. Kamp, I. Sinclair, M.J. Starink, Toughness-strength relations in the overaged 7449 Al-based alloy, Metall. Mater. Trans. A Phys. Metall. Mater. Sci. 33 (2002) 1125–1136, doi:10.1007/s11661-002-0214-2.

[4] L. Zhao, J.G. Santos Macías, L. Ding, H. Idrissi, A. Simar, Damage mechanisms in selective laser melted AlSi10Mg under as built and different post-treatment conditions, Mater. Sci. Eng. A 764 (2019) 138210, doi:10.1016/j.msea.2019.138210.

[5] N. van Dijk, S. van der Zwaag, Self-Healing Phenomena in Metals, Adv. Mater. Interfaces 5 (2018) 1–13, doi:10.1002/admi.201800226.

[6] B. Grabowski, C.C. Tasan, Self-healing metals, in: M.D. Hager, S. van der Zwaag, U.S. Schubert (Eds.), Self-Healing Mater, Springer International Publishing, Switzerland, 2016, pp. 387–408, doi:10.1007/12_2015_337.

[7] V. Srivastava, M. Gupta, Approach to self healing in metal matrix composites: a review, Mater. Today Proc. 5 (2018) 19703–19713, doi:10.1016/j.matpr.2018.06.332.

[8] P.K. Nosonovsky, Rohatgi Michael, Biomimetics in Materials Science, 1st ed., Springer-Verlag, New York, 2012, doi:10.1007/978-1-4614-0926-7.

[9] S. Zhang, N. van Dijk, S. van der Zwaag, A review of self-healing metals: fundamentals, design principles and performance, Acta Metall. Sin. Engl. Lett. 33 (2020) 1167–1179, doi:10.1007/s40195-020-01102-3.

[10] M. Song, K. Du, S.P. Wen, Z.R. Nie, H.Q. Ye, *In situ* electron microscopy investigation of void healing in an Al-Mg-Er alloy at a low temperature, Acta Mater. 69 (2014) 236–245, doi:10.1016/j.actamat.2014.02.004.

[11] H.J. Jeong, M.J. Kim, S.J. Choi, J.W. Park, H. Choi, V.T. Luu, S.T. Hong, H.N. Han, Microstructure reset-based self-healing method using sub-second electric pulsing for metallic materials, Appl. Mater. Today 20 (2020) 100755, doi:10.1016/j.apmt.2020.100755.

[12] X. Ren, Z. Wang, X. Fang, H. Song, J. Duan, The plastic flow model in the healing process of internal microcracks in pre-deformed TC4 sheet by pulse current, Mater. Des. 188 (2020) 108428, doi:10.1016/j.matdes.2019.108428.

[13] G. Siroky, E. Kraker, J. Rosc, D. Kieslinger, R. Brunner, S. Van Der Zwaag, E. Kozeschnik, W. Ecker, Analysis of SN-BI solders: X-ray micro computed tomography imaging and microstructure characterization in relation to properties and liquid phase healing potential, Materials 14 (2021) 1–22 (Basel), doi:10.3390/ma14010153.

[14] M. Arseenko, J. Gheysen, F. Hannard, N. Nothomb, A. Simar, Self-healing in metal-based systems, in: A. Kanellopoulos, J. Norambuena-Contreras (Eds.), Self-Healing Constr. Mater, 1st ed., Springer Nature Switzerland AG, 2022, pp. 43–78, doi:10.1007/978-3-030-86880-2_3.

[15] H. Fang, N. Szymanski, C.D. Versteylen, P. Cloetens, C. Kwakernaak, W.G. Sloof, F.D. Tichelaar, S. Balachandran, M. Herbig, E. Brück, S. van der Zwaag, N.H. van Dijk, Self healing of creep damage in iron-based alloys by supersaturated tungsten, Acta Mater. 166 (2019) 531–542, doi:10.1016/j.actamat.2019.01.014.

[16] S. Hautakangas, H. Schut, N.H. van Dijk, P.E.J. Rivera Díaz del Castillo, S. van der Zwaag, Self-healing of deformation damage in underaged Al-Cu-Mg alloys, Scr. Mater. 58 (2008) 719–722, doi:10.1016/j.scriptamat.2007.11.039.

[17] M. Mahdavi Shahri, R.C. Alderliesten, S. van der Zwaag, H. Schut, Postponing crack nucleation in 2024 aluminium alloy by dynamic precipitation from the supersaturated state, Adv. Mater. Res. 891–892 (2014) 1577–1584, doi:10.4028/www.scientific.net/amr.891-892.1577.

[18] R.N. Lumley, A.J. Morton, I.J. Polmear, Enhanced creep performance in an Al-Cu-Mg-Ag alloy through underageing, Acta Mater. 50 (2002) 3597–3608, doi:10.1016/S1359-6454(02)00164-7.

[19] R. Djugum, R.N. Lumley, D.M. Viano, C.J. Davidson, Enhanced fatigue resistance in a commercial Al-Cu-Mg alloy through underageing, in: Proceedings of the 2nd International Conference on Self Healing Materials,, 2009, pp. 8–11.

[20] R.J.H. Wanhill, Fatigue Crack Initiation in Aerospace Aluminium Alloys, Components and Structures, in: Proceedings of the First International Conference on Self Healing Materials, Springer, 2007, pp. 1–19.

[21] N. Chawla, K.K. Chawla, Metal Matrix Composites, 2nd ed., Springer-Verlag New York, New York, 2013, doi:10.1007/978-1-4614-9548-2.

[22] F. Hannard, A. Simar, E. Maire, T. Pardoen, Quantitative assessment of the impact of second phase particle arrangement on damage and fracture anisotropy, Acta Mater 148 (2018) 456–466, doi:10.1016/j.actamat.2018.02.003.

[23] R. Lumley, Self healing in aluminium alloys, in: S. van der Zwaag (Ed.), Self Healing Materials: An Alternative Approach to 20 Centuries of Materials Science, Springer, 2007, pp. 219–254, doi:10.1007/978-1-4020-6250-6_11.

[24] Z. Balogh, G. Schmitz, Diffusion in metals and alloys, in: Phys. Metall. Fifth Ed., 5th ed., Elsevier, 2014, pp. 387–559, doi:10.1016/B978-0-444-53770-6.00005-8.

[25] R. Bauri, D. Yadav, Processing Metal Matrix Composite (MMC) by FSP, Butterworth-Heinemann, 2018, doi:10.1016/b978-0-12-813729-1.00003-6.

[26] A. Heidarzadeh, S. Mironov, R. Kaibyshev, G. Çam, A. Simar, A. Gerlich, F. Khodabakhshi, A. Mostafaei, D.P. Field, J.D. Robson, A. Deschamps, P.J. Withers, Friction stir welding/processing of metals and alloys: a comprehensive review on microstructural evolution, Prog. Mater. Sci. 117 (2020) 100752, doi:10.1016/j.pmatsci.2020.100752.

[27] J. Villanova, R. Daudin, P. Lhuissier, D. Jauffrès, S. Lou, C.L. Martin, S. Labouré, R. Tucoulou, G. Martínez-Criado, L. Salvo, Fast *in situ* 3D nanoimaging: a new tool for dynamic characterization in materials science, Mater. Today 20 (2017) 354–359, doi:10.1016/j.mattod.2017.06.001.

[28] P. Cloetens, W. Ludwig, J. Baruchel, D. Van Dyck, J. Van Landuyt, J.P. Guigay, M. Schlenker, Holotomography: Quantitative phase tomography with micrometer resolution using hard synchrotron radiation x rays, Appl. Phys. Lett. 75 (1999) 2912–2914, doi:10.1063/1.125225.

[29] G. Martinez-Criado, J. Villanova, R. Tucoulou, D. Salomon, J.P. Suuronen, S. Laboure, C. Guilloud, V. Valls, R. Barrett, E. Gagliardini, Y. Dabin, R. Baker, S. Bohic, C. Cohen, J. Morse, ID16B: A hard X-ray nanoprobe beamline at the ESRF for nano-analysis, J. Synchrotron. Radiat. 23 (2016) 344–352, doi:10.1107/S1600577515019839.

[30] F. Hannard, T. Pardoen, E. Maire, C. Le Bourlot, R. Mokso, A. Simar, Characterization and micromechanical modelling of microstructural heterogeneity effects on ductile fracture of 6xxx aluminium alloys, Acta Mater. 103 (2016) 558–572, doi:10.1016/j.actamat.2015.10.008.

[31] L. Lecarme, E. Maire, A. Kumar, C. De Vleeschouwer, L. Jacques, A. Simar, T. Pardoen, Heterogenous void growth revealed by *in situ* 3-D X-ray microtomography using automatic cavity tracking, Acta Mater. 63 (2014) 130–139, doi:10.1016/j.actamat.2013.10.014.

[32] V. Fallah, B. Langelier, N. Ofori-Opoku, B. Raeisinia, N. Provatas, S. Esmaeili, Cluster evolution mechanisms during aging in Al-Mg-Si alloys, Acta Mater. 103 (2016) 290–300, doi:10.1016/j.actamat.2015.09.027.

[33] G.A. Edwards, K. Stiller, G.. Dunlop, APFIM investigation of fine-scale precipitation in aluminium alloy 6061, Appl. Surf. Sci. 77 (1994) 219–225.

[34] Y. Shen, T.F. Morgeneyer, J. Garnier, L. Allais, L. Helfen, J. Crépin, Three-dimensional quantitative *in situ* study of crack initiation and propagation in AA6061 aluminum alloy sheets via synchrotron laminography and finite-element simulations, Acta Mater. 61 (2013) 2571–2582, doi:10.1016/j.actamat.2013.01.035.

[35] K.S. Toohey, N.R. Sottos, J.A. Lewis, J.S. Moore, S.R. White, Self-healing materials with microvascular networks, Nat. Mater. 6 (2007) 581–585, doi:10.1038/nmat1934.

[36] J.T. Kim, H.J. Kim, S.H. Hong, H.J. Park, Y.S. Kim, Y.J. Hwang, Y.B. Jeong, J.Y. Park, J.M. Park, B. Sarac, W.M. Wang, J. Eckert, K.B. Kim, Thermally-triggered dual *In-situ* self-healing metallic materials, Sci. Rep. 8 (2018) 2–11, doi:10.1038/s41598-018-19936-4.

[37] Z. Li, C. Li, Y. Liu, L. Yu, Q. Guo, H. Li, Effect of heat treatment on microstructure and mechanical property of Al-10%Mg2Si alloy, J. Alloys Compd. 663 (2016) 16–19, doi:10.1016/j.jallcom.2015.12.128.

[38] R. Zamani, H. Mirzadeh, M. Emamy, Mechanical properties of a hot deformed Al-Mg2Si *in-situ* composite, Mater. Sci. Eng. A 726 (2018) 10–17, doi:10.1016/j.msea.2018.04.064.

[39] T.L. Burnett, P.J. Withers, Completing the picture through correlative characterization, Nat. Mater. 18 (2019) 1041–1049, doi:10.1038/s41563-019-0402-8.

[40] S.H. Huo, M. Qian, G.B. Schaffer, E. Crossin, Aluminium Powder Metallurgy, Woodhead Publishing Limited, 2010, doi:10.1533/9780857090256.3.655.

[41] R.M. German, P. Suri, S. Jin, Review : liquid phase sintering, J. Mater. Sci. 44 (2009) 1–39, doi:10.1007/s10853-008-3008-0.

[42] S. Nebti, D. Hamana, G. Cizeron, Calorimetric study of pre-precipitation and precipitation in Al-Mg alloy, Acta Metall. Mater. 43 (1995) 3583–3588, doi:10.1016/0956-7151(95)00023-O.

[43] M.J. Starink, A.M. Zahra, β' and β precipitation in an Al-Mg alloy studied by DSC and TEM, Acta Mater. 46 (1998) 3381–3397, doi:10.1016/S1359-6454(98)00053-6.

[44] W. Wen, Y. Zhao, J.G. Morris, The effect of Mg precipitation on the mechanical properties of 5xxx aluminum alloys, Mater. Sci. Eng. A 392 (2005) 136–144, doi:10.1016/j.msea.2004.09.059.

[45] R. Goswami, P.S. Pao, S.B. Qadri, R.L. Holtz, Severe plastic deformation induced sensitization of cryo-milled nanocrystalline Al-7.5 Mg, Metall. Mater. Trans. A Phys. Metall. Mater. Sci. 45 (2014) 2894–2898, doi:10.1007/s11661-014-2227-z.

[46] R.C. Picu, D. Zhang, Atomistic study of pipe diffusion in Al-Mg alloys, Acta Mater. 52 (2004) 161–171, doi:10.1016/j.actamat.2003.09.002.

[47] G. Yi, A.T. Derrick, Y. Zhu, M.L. Free, A collector plate mechanism-based classical intergranular precipitation model for al alloys sensitized at different temperatures, Metall. Mater. Trans. A Phys. Metall. Mater. Sci. 46 (2015) 5393–5406, doi:10.1007/s11661-015-3110-2.

[48] S.J.L. Kang, Y. Il Jung, Sintering kinetics at final stage sintering: Model calculation and map construction, Acta Mater. 52 (2004) 4573–4578, doi:10.1016/j.actamat.2004.06.015.

[49] K.J. Al-Fadhalah, A.I. Almazrouee, A.S. Aloraier, Microstructure and mechanical properties of multi-pass friction stir processed aluminum alloy 6063, Mater. Des. 53 (2014) 550–560, doi:10.1016/j.matdes.2013.07.062.

[50] L. Choisez, L. Ding, M. Marteleur, H. Idrissi, T. Pardoen, P.J. Jacques, High temperature rise dominated cracking mechanisms in ultra-ductile and tough titanium alloy, Nat. Commun. 11 (2020) 1–8, doi:10.1038/s41467-020-15772-1.